Seismic reservoir characterization of Bone Spring and Wolfcamp Formations in the Delaware Basin — A case study: Part 1

Satinder Chopra[1], Ritesh Kumar Sharma[1], and James Keay[2]

Abstract

The Delaware and Midland Basins are multistacked plays with production being drawn from different zones. Of the various prospective zones in the Delaware Basin, the Bone Spring and Wolfcamp Formations are the most productive and thus are the most drilled zones. To understand the reservoirs of interest and identify the hydrocarbon sweet spots, a 3D seismic inversion project was undertaken in the northern part of the Delaware Basin in 2018. We have examined the reservoir characterization exercise for this dataset in two parts. In addition to a brief description of the geology, we evaluate the challenges faced in performing seismic inversion for characterizing multistacked plays. The key elements that lend confidence in seismic inversion and the quantitative predictions made therefrom are well-to-seismic ties, proper data conditioning, robust initial models, and adequate parameterization of inversion analysis. We examine the limitations of a conventional approach associated with these individual steps and determine how to overcome them. Later work will first elaborate on the uncertainties associated with input parameters required for executing rock-physics analysis and then evaluate the proposed robust statistical approach for defining the different lithofacies.

Introduction

The Permian Basin in west Texas and southeast New Mexico, encompassing an area of approximately 250 (400 km) miles wide and 300 (480 km) miles long, is the most prolific of all the basins in the United States. It has a long history of vertical exploration that dates back to the 1940s when the more permeable conventional reservoirs were being targeted. Advancements in horizontal drilling and hydraulic fracturing opened the low-permeability prospective formations to commercial production and have made Permian production surge to the most productive reservoir in the United States.

The Delaware Basin forms the western subbasin of the Permian, and the Midland Basin forms the eastern part; both are separated by the Central Basin Platform (Figure 1). The Delaware and Midland Basins are multistacked plays with production being drawn from different zones. Of the various prospective zones in the Delaware Basin, the Bone Spring and Wolfcamp Formations are the most prolific and thus the most drilled zones, the combo often being referred to as the Wolf-Bone Play. The northern part of the Delaware Basin is where more horizontal drilling has been carried out in the recent past compared to the southern part, with the latter catching up as well. The pocket that seems like a hot area in the Delaware Basin spans the Ward, Loving, Winkler, and eastern Reeves Counties.

Due to the presence of the evaporites and anhydrites in the shallow sections of the Delaware Basin, the quality of the seismic data appears to be somewhat suboptimum for the characterization of the zones of interest below, namely the Bone Spring, Wolfcamp, Barnett, and Mississippian Formations. Additionally, such characterization is also influenced by lateral and vertical variation of the embedded seismic wavelets in the data, as indicated by the well-to-seismic ties, the absence of shear curves in many of the wells, and the facies complications in the different zones of interest. All of these factors contribute to making the reservoir characterization exercise challenging.

In this study, we try and address the issues mentioned above in the workflow that we generated and we believe that it can be applied to other areas of the Delaware Basin.

3D seismic data acquisition and processing

A 3D seismic survey was acquired for TGS in the Delaware Basin in November 2017 covering 407 mi^2 (1050 km^2) and spanning Ward, Loving, and Winkler Counties in Northwest Texas (Figure 1). The processing of the data was completed in April 2018 and picked up for seismic reservoir characterization that would help in understanding the reservoirs of interest and prove useful toward cost-effective drilling.

[1]Formerly TGS, Calgary, Alberta T2P 0R4, Canada. E-mail: satichop@gmail.com, riteshpes@gmail.com.
[2]TGS, Houston, Texas 77041, USA. E-mail: james.keay@tgs.com.

Manuscript received by the Editor 23 December 2019; revised manuscript received 5 April 2020; published ahead of production 21 June 2020. This paper appears in *Interpretation*, Vol. 8, No. 4 (November 2020); p. 1–14, 24 FIGS.
http://dx.doi.org/10.1190/INT-2019-0294.1.

The acquisition parameters included 165 ft. (50.3 m) for the source and receiver intervals, 660 ft. (201.2 m) for the source-line spacing, 990 ft. (301.8 m) for the receiver line spacing, a maximum offset of 22,756 ft. (6936 m), a 2 ms sample interval, and a 5 s record length, which yielded a bin size of 82.5 ft. × 82.5 ft. (25.2 × 25.2 m). Two vibrator sweeps of 16 s were used as the seismic source. The processing of this large data volume was completed with anisotropic prestack time migration gathers and stacked volume with 5D interpolation made available for reservoir characterization and quantitative interpretation.

The location of the 3D seismic survey is indicated in Figure 1. In Figure 2a, a representative time slice from the 3D seismic volume (1880 ms) is shown that apprises the size and shape of the seismic survey. A representative seismic crossline is shown in Figure 3, giving a glimpse of the quality of the data. The frequency spectra of the seismic data in the upper and the lower half time windows are shown in Figure 2b. Apparently, the frequency bandwidth of the data extends up to 55 Hz in the upper half window and it reduces to 45 Hz in the lower half, with the peak frequency at approximately 15 and 10 Hz, respectively.

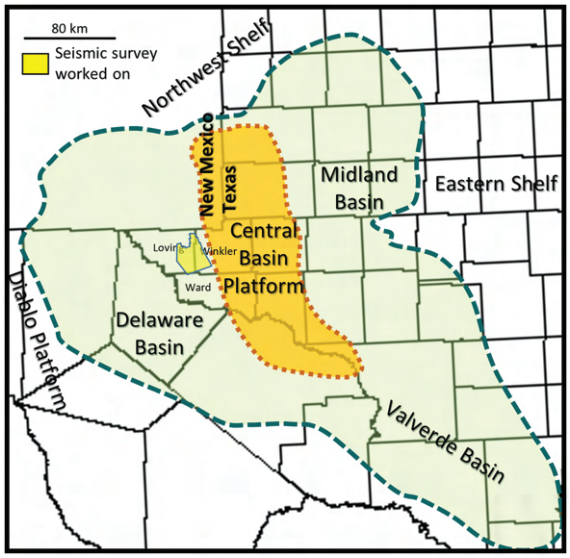

Figure 1. Index map showing the Delaware Basin and the location of the 3D seismic survey.

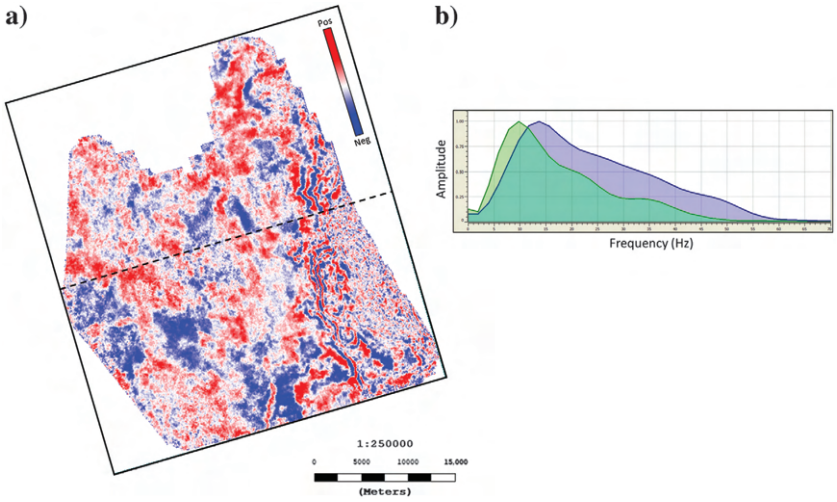

Figure 2. A representative time slice (1880 ms) from the 3D seismic volume. The inlines run north–south, and the crossline runs approximately east–west. (b) The representative frequency spectra for the upper half (blue) and the lower half (green) time window of the seismic data shown in Figures 3.

Geology of the area

The Permian Basin is the largest hydrocarbon-producing basin in the United States. Named after the geologic time during which it reached its maximum depth, it has the world's thickest deposits of Permian rock. Per the EIA (Chapa, 2018), the production from this basin exceeded 3 million barrels per day in 2018. The basin is unique in that it produces from an exceptional number of stacked reservoir zones. The depth of the producing intervals varies from a few hundred meters to more than 6000 m.

Basin development

The Permian Basin comprises the Midland Basin, Central Basin Platform, and Delaware Basin (Figure 1). The deformational sequence of events that controlled these elements is believed to have begun in the Late Precambrian, when widespread tectonic activity affected the North American craton that existed at the time. This led to several high-angle northwest–southeast-trending faults in the Precambrian basement as well as regional lineaments of weakness, which were activated by the later tectonic events. The high-angle basement faults have been mapped (Hills, 1984), and a prominent northwest-trending fault zone is seen at the location of the present Central Basin Platform.

The structural evolution of the Permian Basin can be divided into three stages. The first stage is the early period between the Precambrian and the Mississippian, at which time the Permian Basin was a shallow marine margin at the edge of a vast western sea. During this time, marine carbonates and clastics were slowly deposited.

The second stage is the Pennsylvanian-Permian, when the North American craton collided with the Gondwana Land, which represented a supercontinent at the time, that later split up into South America and Africa. This tectonic activity uplifted the Central Basin Platform and created two asymmetrical deep basins surrounded by shallow margins: the Delaware Basin to the west and the Midland Basin to the east. During this period; clastics, carbonates, and deep-water sediments filled the central parts of both basins, whereas reef complexes grew up along the newly elevated basin margins.

The third stage represents the structural stable phase in the later Permian, at the end of the tectonic activity, when the basins were slowly shut off from the sea and sedimentation took place in a calm, slowly subsiding basinal environment. Evaporation and flooding went on for millions of years, depositing salt precipitates. Reef complexes that developed in the shallow areas were buried by evaporites resulting in an overall sequence of vast marine sediments overlaid by tight strata. The increasing sediment load contributed to basin subsidence, which in turn led to more deposition. Increasing temperature and pressure initiated catagenesis of the kerogens. During the Late Permian, the restriction of the seas became more predominant, resulting in evaporite thicknesses of up to 600 m in the Delaware Basin.

Delaware Basin stratigraphy

The generalized stratigraphic column for the Delaware Basin is shown in Figure 4a. We begin with the Early Ordovician because only limited information on the Cambrian has been recorded from the well data in the Delaware Basin. The Early Ordovician saw deposition of the Ellenburger Formation under broad shelf sea conditions. It consists of gray, medium-grained, crystalline dolomite. The dolomite is siliceous in the lower to middle portion and becomes sandier toward the top. Karstification at the top of the Ellenburger is readily evident on the well-log data. Above the Ellenburger, the Simpson group deposits reach a greater than 600 m thickness in the subsiding basin. It consists of a black shale interbedded with limestone and coarse- to fine-grained sands. Overlying the Simpson group is the Late Ordovician Montoya Formation consisting of cherts and finely grained crystalline carbonates, which are dolomitic and calcitic (Keller et al., 1980).

The rise of the sea level during the Early Silurian unconformably deposited the carbonate sequence of the Fusselman Formation, which is commonly dolomitic. During the Late Silurian and Early Devonian, shelf carbonates were deposited in shallow marine environments and dense limestones, cherts, and black shales were deposited in the deeper basinal areas (Hill, 1996).

The Middle-to-Late Devonian saw a transgressive sea flooding; the basin and black shales of the Woodford Formation were deposited during this time. This fine-grained, highly organic shale formation is an excellent source rock. The thickness varies between 30 and 200 m within the basin, with the thickest deposits found in Winkler County.

The Early-to-Mid Mississippian saw the deposition of Mississippian Limestone. By the later Mississippian, the tectonic activity in the area intensified due to the collision of the Laurasia and Gondwana plates, which ultimately formed Pangea at the beginning of the Pennsylvanian. During the Late Mississippian, the Barnett Shale, which is hard, siliceous, gray to dark-gray, and organic-rich, was deposited.

During the Pennsylvanian, tectonism uplifted the basin flanks causing exposure and erosion, thus depositing mudstones, sandstones, and carbonates. The effects of tectonism in the basin endured through the Pennsylvanian, and there are complex lateral and vertical facies variations in these strata. Formations include the Morrow, Atoka, Strawn, Canyon, and Cisco.

By the late Pennsylvanian, the subsidence of the Delaware Basin increased, resulting in thick Permian sediments in the basin center, whereas the shelf areas remained a shallow carbonate bank environment. The

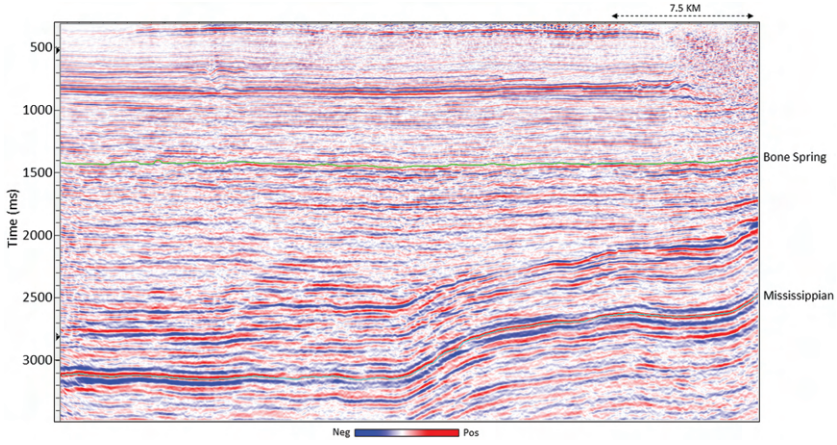

Figure 3. A representative crossline section from the seismic data volume, with Bone Spring and Mississippian markers tracked on it. The quality of the seismic data is reasonably good.

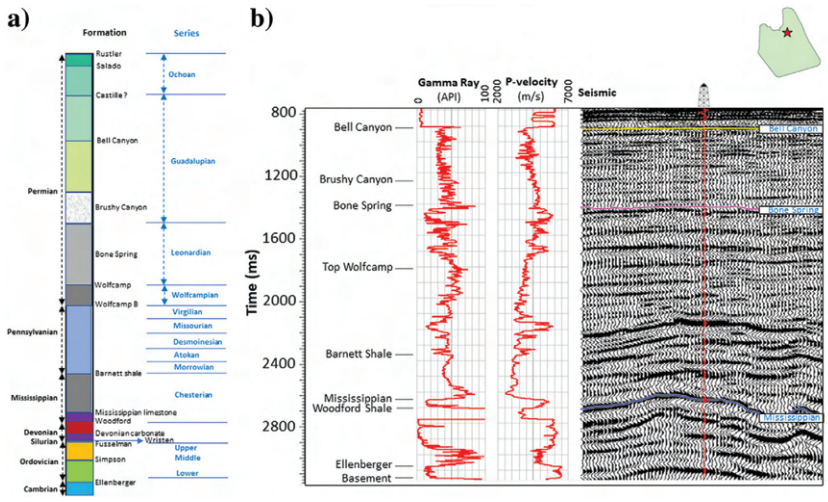

Figure 4. (a) Generalized stratigraphy of the Delaware Basin and (b) correlation of well curves for a deep well on West Kermit 3D with seismic data. As the well extends down up to the basement, the different lithounits can be read off the formation tops and located on the seismic section.

Permian strata have been divided into four series based on lithology and fossil content (Adams et al., 1939), namely, Wolfcampian, Leonardian, Guadalupian, and Ochoan.

During the Wolfcampian, dark shale and limestone with silt and sand zones characterize the central parts of the basin and carbonate buildups and banks on the shelf areas.

The Leonardian saw continuing subsidence of the Delaware Basin, though somewhat slower than the Wolfcampian. The Leonardian Series consists of the Bone Spring Formation, with sequences of dark-gray deep-marine shales interbedded with sands and black limestones. The thickness of the Bone Spring Formation varies from 700 to 1000 m, which was deposited in three different cycles, separated by carbonate sequences. Whereas the sands were deposited as turbidities during low sea levels, the black bituminous-rich limestones were deposited in deep euxinic basinal environments. These units, in particular the Avalon shale, may contribute as source rocks in the Delaware Basin.

A thick column of siliciclastics, the Delaware Mountain Group, was deposited over the Bone Spring Formation during the Guadalupian, with continual subsidence of the basin. The members of this series are the Brushy Canyon, Cherry Canyon, and Bell Canyon, which reach a maximum thickness of 1500 m in the center of the Delaware Basin. The sandstones in this series make good reservoirs, and significant oil production has been allocated to the stratigraphic traps in the Bell Canyon. These basinal deposits are time equivalents to the Capitan and Goat Seep reef complexes exposed in the Delaware Mountains.

During the Late Permian, the Delaware Basin was closed to the marine waters; thus, the Ochoan Series saw the deposition of the evaporates and thin red beds that onlapped and eventually buried the Permian reefs. The members of this series are the Castille (anhydrite), Salado (halite), Rustler (dolomite), and the Dewey Lake (continental red bed) Formations.

With the above geologic information in mind, a deep well was selected over the 3D seismic volume (the location is indicated in Figure 4b) and the well curves were correlated with the seismic data. The different lithounits were identified on the log curves with the available formation tops, and the equivalent intervals were identified on the seismic data. We found that whereas the Mississippian, Bone Spring, and Bell Canyon were found to be trackable on the seismic data, other horizons such as Wolfcamp (along with its subunits) and Barnett were not easily trackable. The extent of the broad zone of interest extends from the Bell Canyon (close to 800 ms) to Mississippian (close to 2800 ms), an overall interval of 2 s.

In Figure 5 we focus on the "WolfBone" and its two main lithounits of interest, i.e., the Bone Spring and the Wolfcamp zones. The subunits within Bone Spring Formation (first, second, and third Bone Spring sands and carbonates) and Wolfcamp (A, B, and C) are indicated, and these are prospective and thus represent the zones of our interest.

Well-to-seismic ties

Tying seismic data to the available well control is a crucial step in seismic interpretation, an important component of seismic reservoir characterization. The subsurface reflection coefficient series can be calculated from the impedance well-log curves, but to generate a 1D synthetic seismogram, the reflectivity must be convolved with a wavelet. For this purpose, the wavelet can be extracted from the seismic data statistically or deterministically by comparing it with the seismic trace at the location of the well. This way, the generated synthetic seismogram can be correlated with the seismic data. In practice, this process comes with its own issues.

Usually, a single wavelet is extracted in a time window for the generation of the synthetic seismogram under the assumption of stationarity of the seismic data. In such a case, the reflection events of the seismic may match in the chosen time window but may not exhibit a good match above or below that zone. This mismatch will be particularly emphasized if a large time window is chosen for wavelet extraction because the seismic data are generally nonstationary due to the various propagation effects that the seismic waves go through in the subsurface. Added to this is the noise contamination of the seismic data. One of the propagation effects is anelastic attenuation that makes the seismic data continuously lose frequency and cause changes in its phase with time. Due to this, the

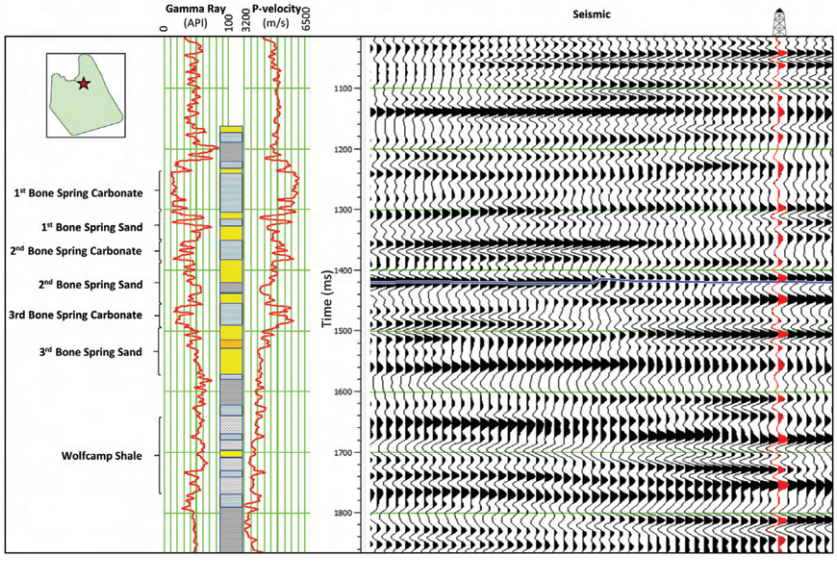

Figure 5. The stratigraphic column of the Delaware Basin focused on the Bone Spring and Wolfcamp intervals and its correlation with seismic data.

"very notion of a single wavelet is not robust" (Margrave, 2013). Correction for the anelastic attenuation propagation is usually done during the processing of seismic data by performing inverse-Q filtering, which requires a knowledge of Q values as a function of time. The application of an appropriate Q correction to seismic data leads to a time-variant amplitude balancing of the data in frequency and residual phase. But because the required Q values are usually not available, either inverse-Q filtering is not performed at all or a constant-Q inverse-Q filtering is applied over a large time window by guessing the Q value for its application. On checking the processing sequence of the seismic data in hand, it was found that indeed no inverse-Q filtering had been performed on the data.

As mentioned above, a single wavelet in a large time window would result in reflection event mismatch above and below the time window chosen for wavelet extraction and in the flawed formation calibration as well. If such a wavelet is used for performing seismic impedance inversion, it could possibly result in missing geologic features or it could subsequently result in inaccurate estimation of rock properties. In the present exercise, because the time window spanning Bone Spring to Mississippian is more than 2 s long, the idea of extraction of a single average seismic wavelet over that window was not considered advisable, and so it was abandoned.

Seismic wavelets were extracted in overlapping (10%) time windows at different well locations over the 3D volume, and their frequency spectra were computed. In Figure 6a–6c, we show a comparison of three such representative wavelet suites, where we notice a variation in the temporal as well as the spatial directions. For simplicity, their average was computed (Figure 6d), which yielded a single time-varying wavelet and was used for synthetic seismogram generation at the different well locations.

The spatial variation in the wavelet shapes is expected, as the wells to the right side of the survey, due to their proximity to the Central Basin Platform, should exhibit some differences from the wells to the left side of the survey. We consider this spatial variation in the wavelet shape and frequency content during simultaneous impedance inversion and will be discussed later.

In Figure 7, we show the input sonic, density, and gamma-ray well-log curves in red for well W3 (Figure 6), with its smoothed version used in the analysis overlaid in dark blue. The generated synthetic seismogram in blue is shown correlated with seismic data in red, with the red trace in the seismic segment exhibiting the location of the well. The frequency variation on the synthetic traces is evident, and so also on the seismic data as expected. A segment of an arbitrary line through the 3D seismic volume and passing through the different wells to the left as indicated in Figure 6 are exhibited in Figure 8. The synthetic seismograms have been inter-fixed in the arbitrary line in color. The correlation between them seems to be reasonably good.

Low-frequency model building

For the generation of an impedance field using well-log data, the usual practice is to apply a low-pass filter (<10 Hz) to the available sonic well-log curves and use one or more of the derived curves for generation of the interval velocity field using extrapolation or interpolation and guided by horizon boundaries. Where more than one well is used for the generation of the interval velocity field, usually an inverse-distance weighted scheme or a process called kriging is used. Such techniques should be used with care because they can produce artifacts in the form of artificial tongues of sharp velocity changes that are nongeologic.

Instead of using such a technique that could be fraught with problems, we make use of a relatively new approach for the generation of an interval velocity field that utilizes well-log data and seismic data to establish the relationship between seismic attributes and the well-log curves. In this approach, the low-frequency velocity model generated with a single well is used as one of the inputs, and some other seismic attribute data volumes. A multiregression approach (Ray and Chopra, 2016) is used, wherein a target interval velocity log is modeled as a linear combination of several input attributes at each sample point. This results in a series of linear equations that are solved by obtaining a linear-weighted sum of the input seismic attributes in such a way that the error between the predicted and the tar-

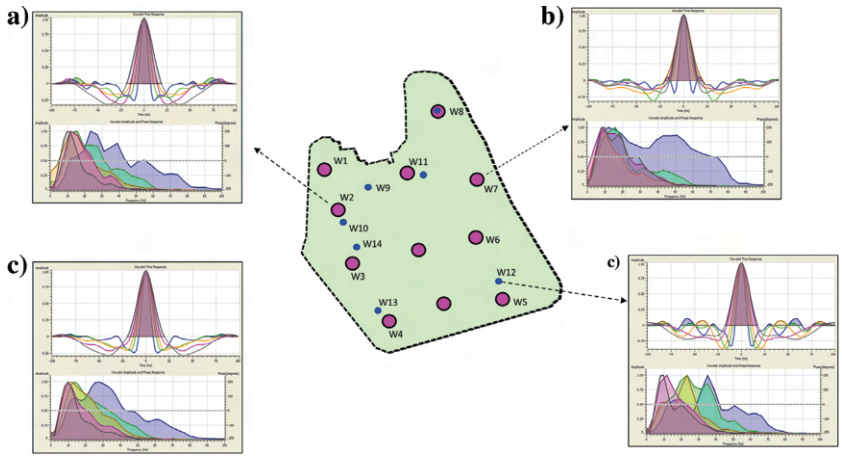

Figure 6. Base map showing the location of the available wells on the 3D seismic survey. Wavelets were extracted at the well locations indicated with the dashed arrows in time-varying overlapping windows as are shown in (a-c), along with their frequency spectra. Notice the change in the shape of the wavelets and their frequency content from left to right. The average of the time-varying wavelets at the wells shown on the base map is shown in (d), which seems to be more stable.

get log is minimized. The workflow for the method is illustrated in Figure 9. In the case at hand, we extended this approach to include two wells (W3 and W7) so as to capture the varying geologic trend from east to west. We determine the correct number of attributes to use by what is referred to as a cross-validation method (Hampson et al., 2001). Whereas the additional attributes always improve the fit to the training data, they may be useless or worse when applied to new data not in the training set. In the process of cross-validation, one well at a time is excluded from the training data set and the prediction error is calculated at that well. The analysis is repeated as many times as there are wells, each time leaving out a different well. The total validation error is the root-mean-squre (rms) average of the individual errors. Thus, in addition to the low-frequency volume generated with the two wells as mentioned above, the relative acoustic impedance volume, seismic velocity volume, the input seismic and its band-pass-filtered version 5-10-15-20 were used as inputs. The choices for the number of seismic attributes as well as the operator length to be used in the multilinear regression analysis are based on prediction error analysis. The length parameter estimates the target low-frequency log by using an ensemble of seismic samples on each attribute. The minimum error was sought for both seismic attributes and the length parameter, and it was found to be 5 and 9, respectively, for our exercise. A cross-validation analysis between the measured and the predicted impedance formed part of the workflow. It showed a high correlation coefficient, which lent more confidence to the whole process. More details can be found in the references cited above.

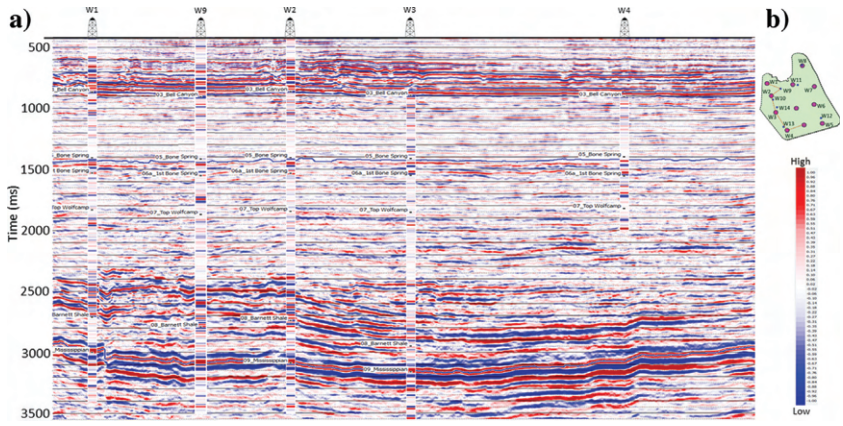

Figure 8. An arbitrary line through the seismic volume passing through nine different wells as shown on the base map (top right). The segment of the arbitrary line marked in red and passing through five wells is shown in (a), and the second half of the arbitrary line marked in blue is shown in (b). Synthetic seismograms generated at the well locations are shown interfixed on the arbitrary line segments. Notice that the correlation between the two is reasonably good.

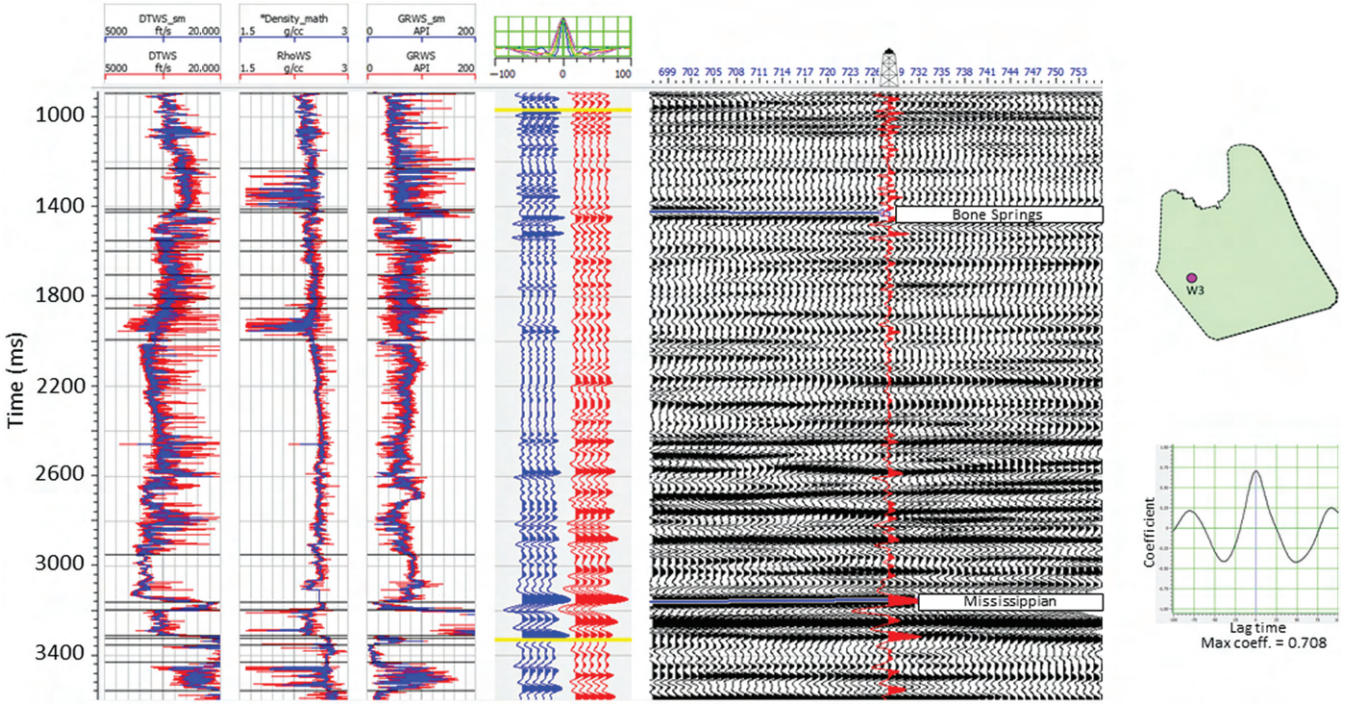

Figure 7. Synthetic seismogram generation for well W3. The input well-log curves sonic, density, and gamma ray (in red) and their smoothed versions in blue are shown to the left. The synthetic seismogram in blue is generated using the sonic and density curves and the wavelets extracted in overlapping time windows. It is correlated with the seismic traces in red. The correlation coefficient is 0.708, which is much better than correlating a synthetic seismogram generated with a single wavelet.

Estimation of shear curves

Along with the compressional velocity and density, the shear wave velocity is a useful parameter that is required for the determination of the lithology, pore fluid, and other geomechanical parameters of the formations of interest. Seismic data applications such as amplitude variation with offset (AVO) or prestack simultaneous impedance inversion require shear velocity information for generation of input models that are then used for the determination of shear impedance. This is then carried forward for the determination of parameters such as V_P/V_S, lambda-rho, mu-rho, and E-rho, where E is the Young's modulus, which can be used for the determination of the lithology, fluid, or other rock mechanics parameters.

The shear-wave velocity is measured directly in the borehole with a dipole shear tool, but it is usually not available in all of the wells used for analysis in a project. The reasons for the nonavailability of the shear log curves in wells vary from the old wells not having them to the cost associated with their acquisition. In the interest of economics again, many oil companies do not continuously record shear log curves over the length of the wells, where the sonic or other curves may be acquired. Consequently, shear curves are commonly recorded over short intervals in wells.

Different workers have suggested the use of empirical (Castagna et al., 1985; Greenburg and Castagna, 1992) or theoretical (Krief et al., 1990) relationships for estimation of shear velocity from the available compressional velocity information. Such computations were initially suggested for sandstones, which may or may not be generalized for every subsurface formation. Also, recognizing the fact that the relationship between the compressional and shear velocity may not be a straightforward linear one, other workers have demonstrated the use of multilinear regression and artificial neural networks for shear velocity well-log estimation by making use of other well curves. Generally, it is found that better correlations exist between the shear curves estimated by way of these methods and the measured shear curves used as blind wells, than a simple application of an empirical relationship such as Castagna et al. (1985) or Greenburg and Castagna (1992). Well-log curves such as sonic, gamma-ray, neutron-porosity, density, and resistivity are usually available over longer depth intervals and could be used as input for the training of neural networks on log data from one or more wells where shear curves are available. After cross-validation analysis, shear curves were generated over longer intervals or for the complete estimation in the broad zone of interest.

For the 3D dataset at hand, three wells (W4, W12, and W9 in Figure 10) were available with shear curves in addition to sonic, gamma-ray, resistivity, and porosity, over an interval from Bell Canyon to Mid-Wolfcamp.

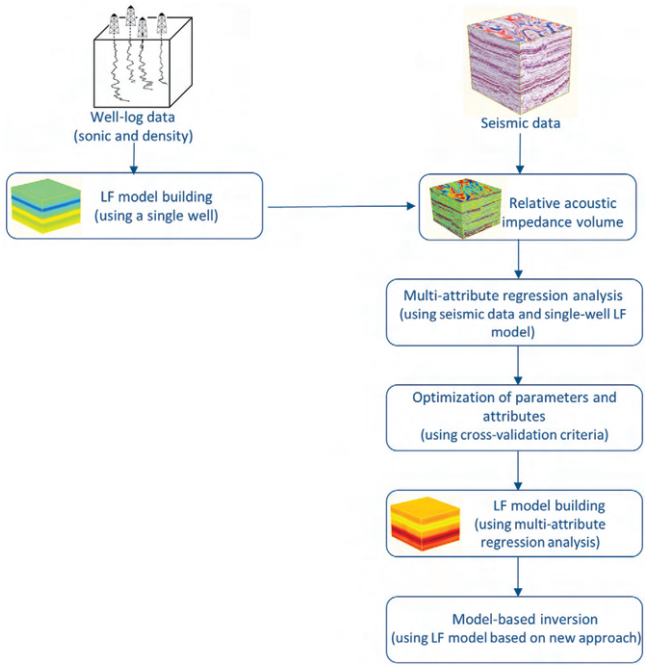

Figure 9. Workflow for generating low-frequency model using multiattribute regression approach. Besides the low-frequency model using wells W3 and W7, the seismic velocity, relative acoustic impedance derived from the input seismic data, and band-pass-filtered version of the seismic data were used for the multilinear regression analysis.

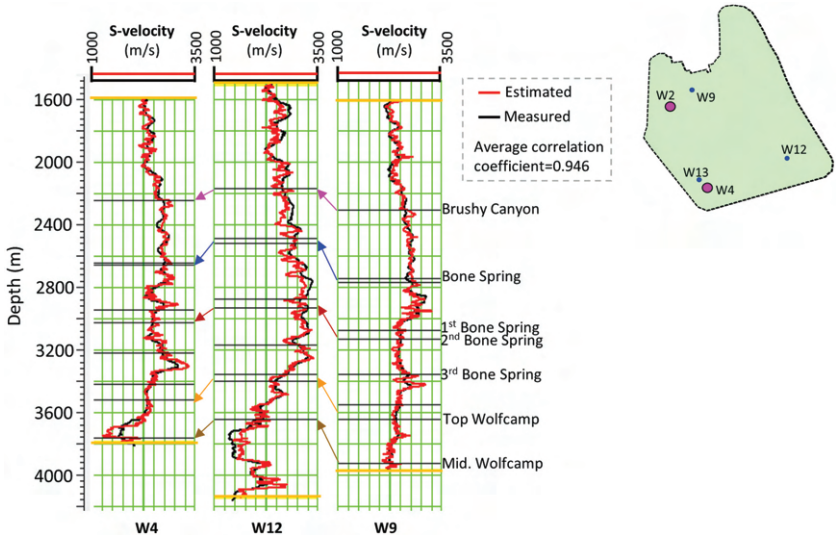

Figure 10. The estimated shear curves in red at three wells (W4, W12, and W9) overlaid on the measured shear curves in these wells. The depth interval depicted on the displays is between the Brushy Canyon and Mid Wolfcamp. The well-log curves used in the neural net training are the P-wave, gamma-ray, resistivity, and porosity. The average correlation coefficient for the three wells is 0.946, which is very encouraging.

The neural networks were trained on these wells followed by cross-validation analysis. Thereafter, shear curves were predicted for wells W13 and W2, which were not used in the training of the neural networks. Whereas well W13 had measured shear curve from Bell Canyon to Mid-Wolfcamp, well W2 had this curve for Mid-Wolfcamp to Barnett.

A good correlation was found between the multilinear regression-estimated shear velocity and that measured in the two blind wells as shown in Figure 11. In the present study, the impedance inversion is to be carried out from Bone Spring to Mississippian, and because shear curves are not available over such large intervals, confidence in the estimated shear curves over Bell Canyon to Mid-Wolfcamp and from this level to Barnett (Figure 11b) helped us proceed with the estimation of shear curves for all of the deep wells that had sonic and density curves. A crossplot of P- and S-impedance was generated for all of the deep wells, wherefrom a linear relationship was determined, which was then used to generate the shear-wave low-frequency impedance model for simultaneous impedance inversion. Besides this important application, the estimation of shear information as discussed above plays a very crucial role in lithologic trend analysis as discussed later.

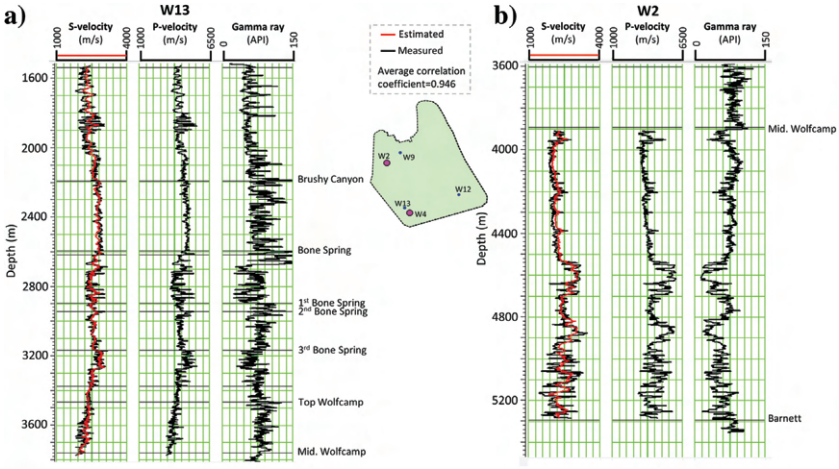

Figure 11. (a) The estimated shear curves in red overlaid on the measured shear curve in black for blind well W13. The depth interval depicted on the displays is between the Brushy Canyon and Mid Wolfcamp. (b) The estimated shear curve (in red) overlaid on the measured shear curve (in black) in the other blind well W2, for the depth interval Mid Wolfcamp to Barnett.

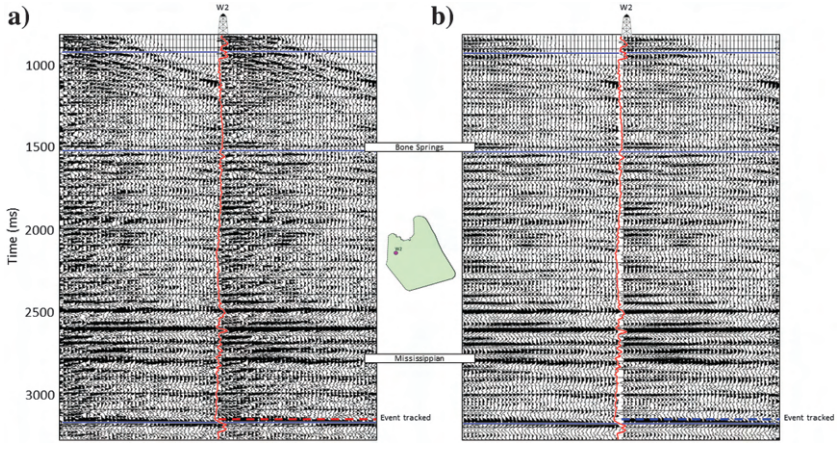

Figure 12. Two representative (a) input seismic gathers and (b) the equivalent preconditioned supergathers, around the W2 well. The location of the well is indicated on the map in the inset, which is to the right side of the survey and close to the Central Basin Platform. Notice the enhancement in the S/N ratio after conditioning.

Preconditioning of seismic data

The seismic data were conditioned carefully to make sure that amplitudes are preserved such that their variation with offset/angle could be used in a meaningful way. The major processes employed in the conditioning were supergathering (3×3), band-pass filtering, random-noise attenuation, and trim statics, with difference plots taken at each step to ensure that no useful signal was distorted or attenuated. In Figure 12, we show the comparison of a couple of input gathers at the location of well W2 before preconditioning, with the equivalent supergathers after preconditioning. Notice the noisy appearance of the input gathers where the somewhat weaker reflection signal appears to be drowned in the background of the noise (Figure 12). The signal-to-noise ratio (S/N) seems to have been much improved on the equivalent preconditioned supergather shown in Figure 12b, and the weaker reflections are also clearly seen.

An important quality control during preconditioning of prestack seismic data is to ensure that the variation of amplitude with offset/angle does not change as the data go through preconditioning. To ensure this, in Figure 13, we show amplitudes at selected events plotted as a function of offset before and after preconditioning. We notice that the scatter of amplitude values after preconditioning is reduced, but the overall gradient remains the same.

Offset-to-angle transformation

Whereas seismic data are acquired and processed in the offset domain, AVO analysis or simultaneous inversion is performed in the angle domain. Usually, for the transformation of offsets into angles, the following relationship given by Walden (1991) is utilized:

$$\mathrm{Sin}\theta = \frac{V_{\mathrm{int}}x}{V_{\mathrm{NMO}}^2 t} = \left(\frac{V_{\mathrm{int}}}{V_{\mathrm{Smooth}}}\right)\frac{x}{\sqrt{x^2 + (V_{\mathrm{Smooth}}t_0)^2}}, \quad (1)$$

where V_{int} is the interval velocity obtained from V_{Smooth} and V_{Smooth} is the spatially varying velocity derived by smoothing the stacking velocities over a cable length (Mukhopadhaya and Mallick, 2011).

Per the above equation, it can be concluded that velocity plays an important role in domain conversions.

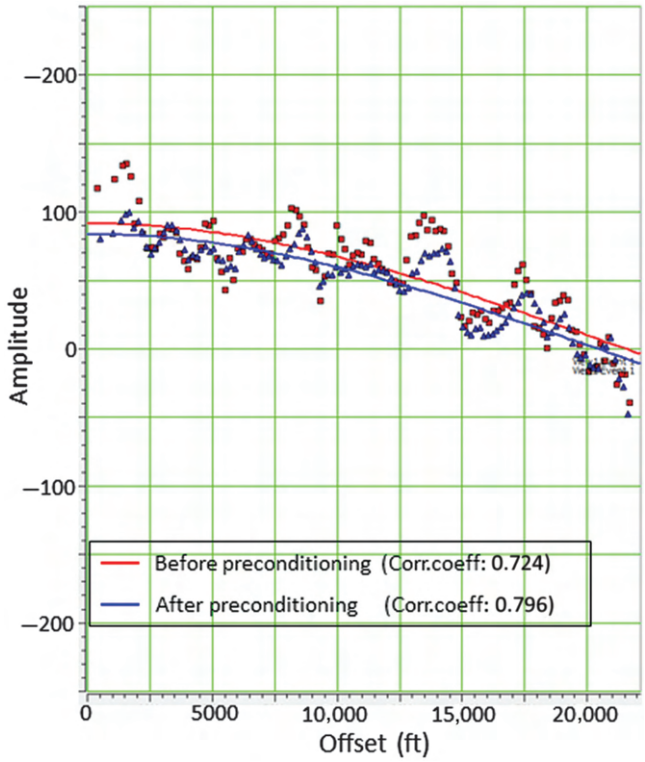

Figure 13. Amplitude analysis at reflection events shown in dashed red on the seismic gather before conditioning, and in dashed blue on the preconditioned gather in Figure 12. The scatter of points after conditioning is reduced, but the overall gradient remains the same.

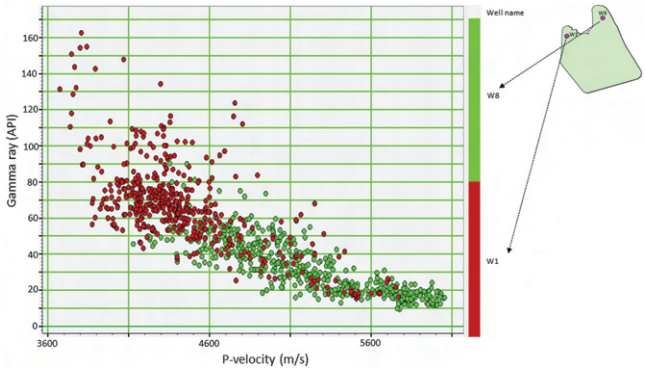

Figure 14. Crossplot of the P-velocity and gamma ray for wells W1 and W8 as indicated on the base map. A more pronounced clustering of points is seen to the left and right halfs of the crossplot.

Two types of velocities, namely, seismic and well velocity, are available for analysis. During the processing of seismic data, the velocity analysis yields the rms velocity field. This velocity field can then be converted into an interval velocity field using Dix's (1955) hyperbolic approximation relationship, which, besides knowledge of the rms velocity, requires the two-way traveltime at zero offset. Usually, the seismic velocity has its own limitations due to limited resolution and not necessarily being horizon-consistent.

As well velocity is considered as the ground truth measurement, it is tempting to use it for domain conversion. However, it needs to be decided whether a single well would be sufficient to represent the whole 3D seismic volume or if more wells need to be considered in the analysis.

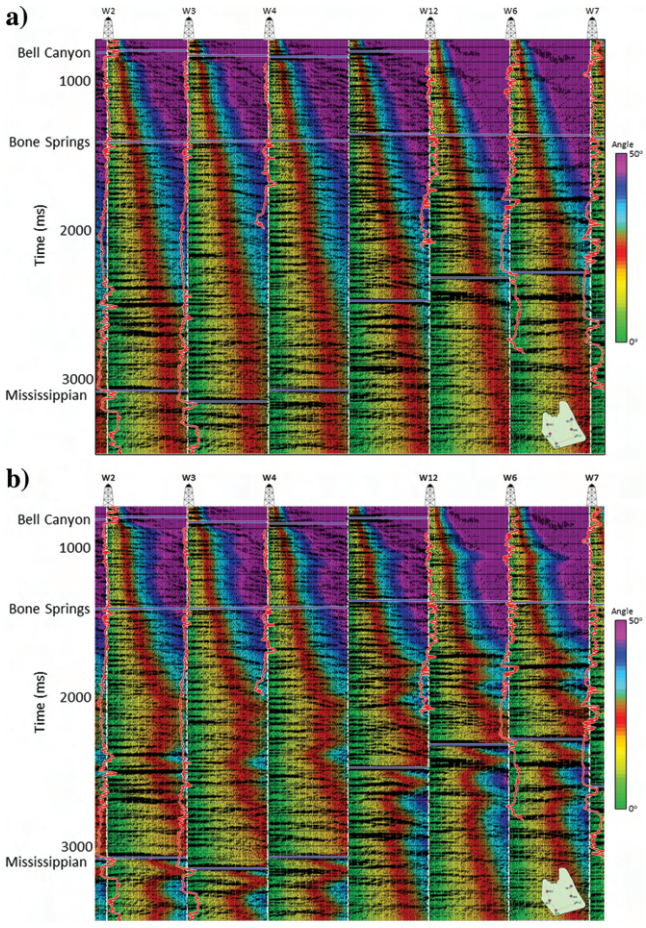

Figure 15. The angles of incidence computed using the (a) seismic interval velocities and (b) velocity field generated using the available well data via multiattribute regression analysis, overlaid on seismic offset gathers. The gathers are selected along an arbitrary line passing through some well indicated at the top of the sections. The sonic velocity curves have been overlaid at the well locations. Notice the gradual changes in the angle of incidence in (a), whereas in (b) there are sharp changes in the angles of incidence seen at the Mississippian level, and even at the other reflectors coinciding with the sharp increases on the sonic log.

As we began analyzing the available well-log data, we came across an interesting observation. On the crossplots of P-velocity and gamma-ray, there were distinct differences in terms of the cluster density of points, for wells to the western and eastern side of the survey. Figure 14 shows a crossplot between the P-velocity and gamma-ray for a pair of wells to the north, namely, W1 and W8. The time window for the points crossplotted is Bone Spring to Top Wolfcamp. The point cluster in red comes from well W1, and those in green come from well W8. Notice the pronounced separate clustering of the red and green points on the crossplot. Similar observations were made for the two other pairs of wells that were examined. These crossplots suggest significant differences in velocity and gamma ray between the wells on the western and eastern sides of the survey.

Hence, multiple wells should be considered in the velocity model-building process. But, as mentioned earlier, the use of multiple wells brings its own problems in the analysis and needs to be used carefully. Therefore, we followed the multiregression approach as discussed earlier. We thus generated the angle of incidence values at each gather using the seismic interval velocity field and the well interval-velocity field and compared them by overlaying them on the seismic offset gathers shown in Figure 15.

We make an interesting observation here. Normally, seismic velocity picking is done by following an increasing trend, so that the interval velocities obtained after conversion and smoothing also exhibit a smooth trend with increasing time. When such an interval velocity field is used for offset-to-angle transformation, and the latter is overlaid on seismic offset gathers in color, even in the presence of a sharp contrasting interface in the subsurface, the angle of incidence does not exhibit any appropriate change there. We exhibit this observation in Figure 15a, where the angle of incidence is overlaid on preconditioned seismic offset gathers. Notice that, at the level of the Mississippian marker especially, there is no change in the angle of incidence. In Figure 15b, we show the section equivalent to the one shown in Figure 15a, where the computed angle of incidence using well data is overlaid on the seismic offset gathers. Note that, not only are there changes seen at the Mississippian marker, but even at other levels that coincide with sharp increases on the impedance log, changes in the angle of incidence are noticed as expected.

Due to this convincing observation, we went along with the angle-of-incidence computation using well-log data.

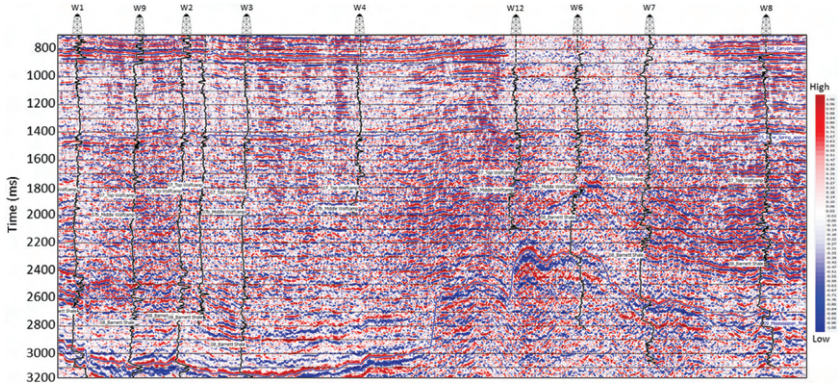

Figure 16. Near-angle stack section along an arbitrary line.

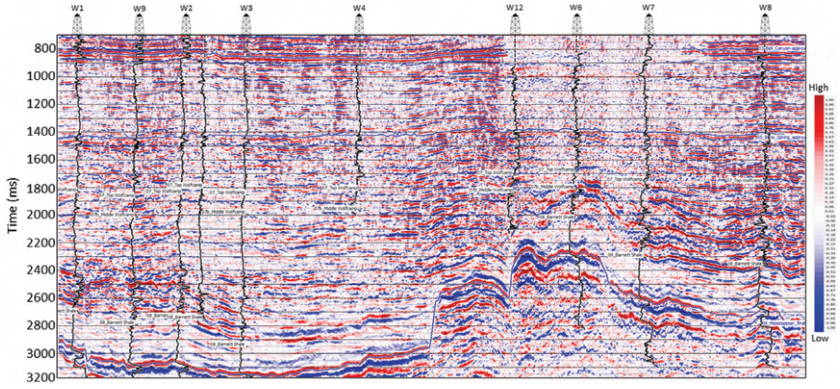

Figure 17. Mid1-angle stack section along the same arbitrary line shown in Figure 16.

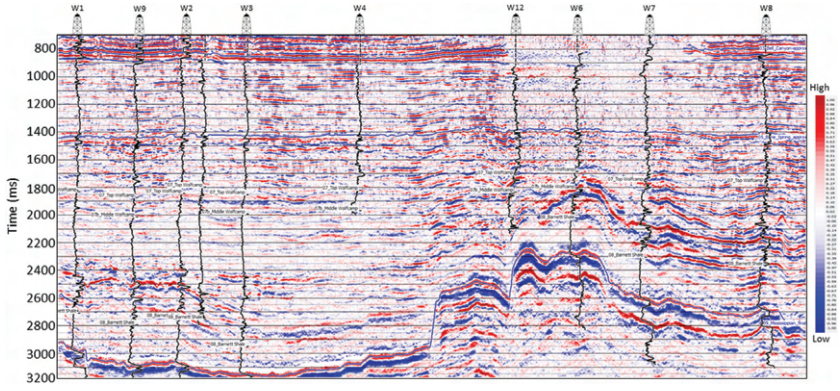

Figure 18. Mid2-angle stack section along the arbitrary line.

Prestack simultaneous impedance inversion

In simultaneous prestack inversion, multiple partial-offset or angle substacks are inverted simultaneously. For each angle stack, a unique wavelet is estimated.

Subsurface low-frequency models for the P-impedance, S-impedance, and density constrained with the appropriate horizons in the broad zone of interest are constructed using the approach explained above. The models, wavelets, and partial stacks were used as input in the inversion, and the output was P-impedance, S-impedance, and density. The mathematical formulation for the present implementation of prestack simultaneous impedance is described in Hampson et al. (2005).

Quality control of data going into simultaneous impedance inversion

Dealing with noisy near-angle stack data

Once the angle gathers were generated for the seismic volume, four different angle substacks near (0°–9°), mid1 (9°–18°), mid2 (18°–27°), and far (27°–36°) were generated. On examination, the near-angle stack was found to be noisier than the other angle stacks. Per our experience in working with projects in the Midland Basin, we had made similar observations. In Figures 16–19, we exhibit an arbitrary line passing through the different wells shown therein from the near-angle stack, mid1, mid2, and the intercept stacks. Notice the much lower S/N of the near-angle stack compared with the other two. When noisier near-angle stacks are used in the impedance inversion, the computed P- and S-impedance data are found to have a low S/N. To avoid this, we weighed in on a couple of options, such as leaving out the near-angle stack or replacing it with the intercept stack computed using a two-term Aki-Richards equation.

We carried out P-impedance inversion when the near-angle stack was used in the inversion, next when it is not used, and finally when it is replaced with the intercept stack, respectively, and correlated with the different wells. We found better continuity of events and correlation with the P-impedance log curves, when the intercept stack was used in place of the near-angle stack.

We thus decided to replace the near-angle stack with the intercept stack in the simultaneous inversion.

Dealing with different lithological trends in the zones of interest

Realizing that the zones of our interest in 3D seismic data at hand span through the Bone Spring, Wolfcamp, Barnett Shale, and Mississippian Formations, a key question to answer is, Which background trend should be considered in the inversion? Would a single trend be adequate for defining the background trend? In a thin zone picked up for impedance inversion where a reservoir does not have facies complications, the above suggestion is good. However, facies complications exist in the area of study and different facies may have different background trends. Thus, it may not be appropriate to use only a single background trend in the impedance inversion. To deal with such a scenario, the following approach is proposed.

We begin with crossplotting the P-impedance, S-impedance, and density using available well-log data over the formations of our interest, and we search

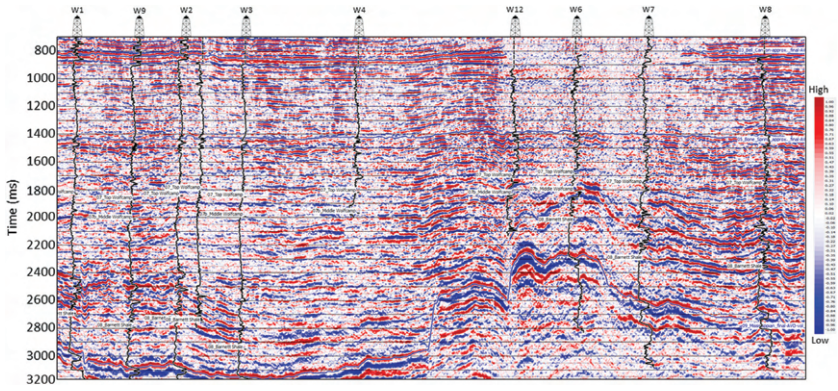

Figure 19. Intercept stack section along the arbitrary line.

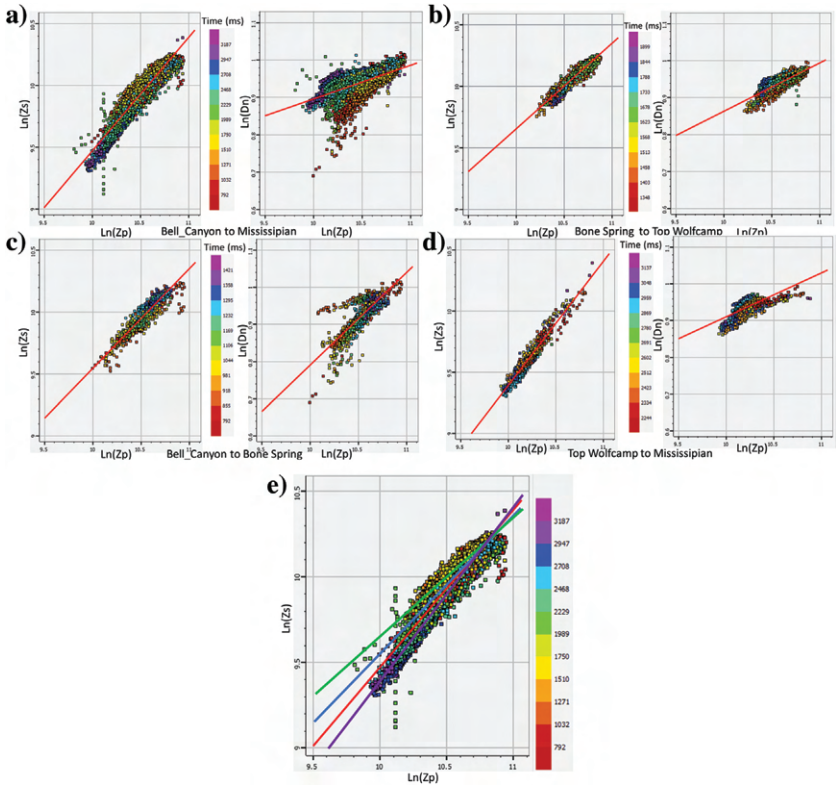

Figure 20. Lithological trend analysis in terms of crossplots to be used in impedance inversion in different lithointervals: (a) Bell Canyon to Mississippian, (b) Bell Canyon to Bone Spring, (c) Bone Springs to Top Wolfcamp, and (d) Top Wolfcamp to Mississippian. (e) The different trends overlaid on one crossplot.

for existing trends in the crossplot space for optimization of the inversion. We believe that the above approach is a better way of handling the facies complication problem rather than following an approach that starts with different facies trends in the low-frequency domain. The problem associated with the latter approach is that of defining the different facies before running the inversion, a calibrated petrophysical model is required, which most of the time is not available. Another concern about this approach is that unconventional plays, such as the present one, may have different types of shale characteristics (laminated, dispersed, or structural), and it is not well documented if all these shales possess the same compaction trend or different ones.

Following our approach, in Figure 20a–20d, we exhibit crossplots between $\ln(I_P)$ and $\ln(I_S)$ as well as between $\ln(I_P)$ and $\ln(\rho)$ for individual intervals comprising (1) the overall zone from Bell Canyon to the Mississippian, (2) Bone Spring to Top Wolfcamp, (3) Bell Canyon to Bone Spring, and (D) Top Wolfcamp to Mississippian. When such a crossplot is constructed for the overall zone (Bell Canyon to Mississippian), four different trends can be drawn through the cluster points (Figure 20e), suggesting a separate trend for each of the intervals of interest.

This significant observation prompted us to not carry out simultaneous inversion in a large time window using a single average rock physics or facies trend. We therefore decided to carry out simultaneous impedance inversion in individual lithounits, comprising Bone Spring to Top Wolfcamp, Top Wolfcamp to Mississippian, etc., and merge these impedance intervals into a composite volume.

In Figure 21, we show a segment of an arbitrary line passing through two wells (W14 and W6) drawn from the S-impedance volume generated using a single trend for the complete zone shown. In Figure 22, we show the equivalent section from the S-impedance volume when different trends were used for the constitutive intervals. Notice the difference between them as indicated within the highlighted pockets. Similar comparisons were carried out for the sections drawn from the V_P/V_S data volumes, and valid differences were noticed.

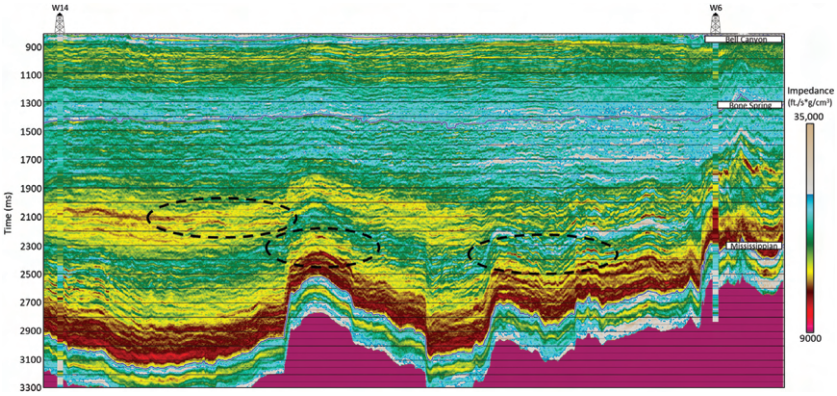

Figure 21. Inverted S-impedance section along the arbitrary line when a single trend is used in the inversion analysis.

Spatial variation of wavelets

Earlier, we saw significant differences between the crossplots generated be-

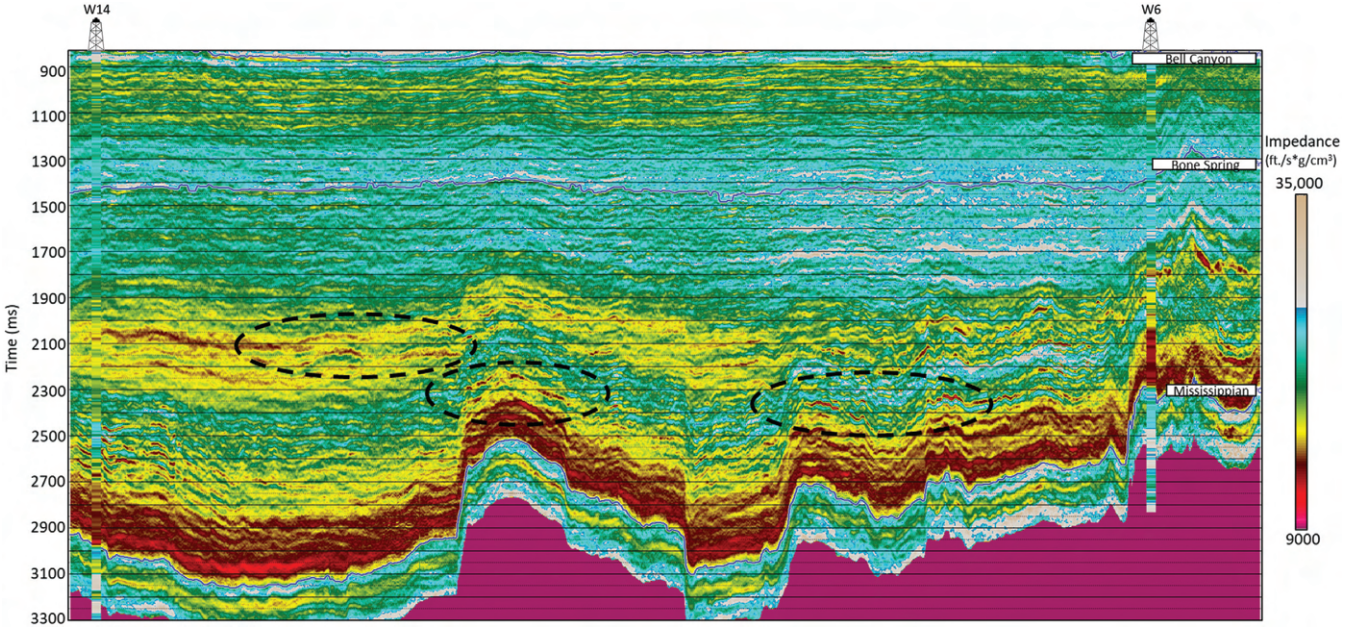

Figure 22. Inverted S-impedance section along the arbitrary line when different trends are used for different zones in the inversion analysis.

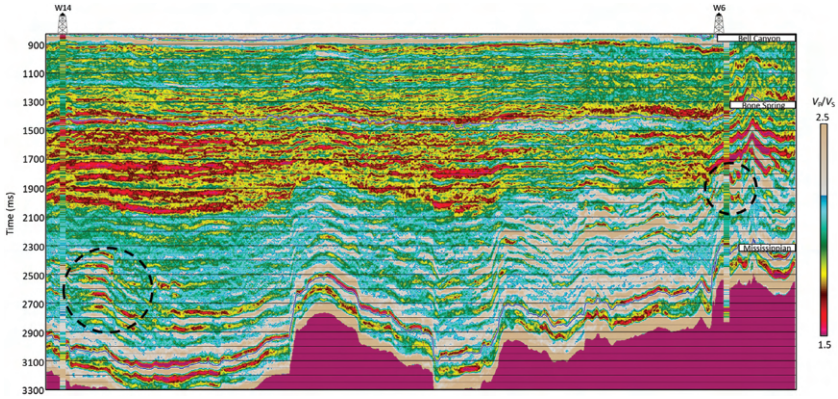

Figure 23. Inverted V_P/V_S section along the arbitrary line when different trends are used for different zones in the inversion analysis *without* spatial varying wavelet.

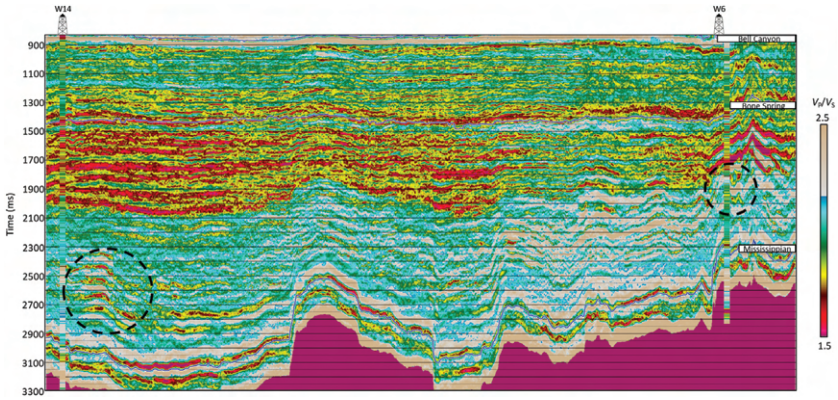

Figure 24. Inverted V_P/V_S section along the arbitrary line when different trends are used for different zones in the inversion analysis *with* spatial varying wavelet.

tween the P-velocity and gamma ray for pairs of wells, one to the west and the other to the east. Also, on examining the different angle stacks, we found spatial changes in the reflection detail. The segment of the arbitrary line to the east has higher amplitude reflections, whereas to the west, low-amplitude reflections are observed. Similarly, as seen earlier, the extracted wavelets in the wells to the east and west show variations (Figure 6). All of these observations are suggestive of the fact that there would be spatial variations in the seismic wavelets. We therefore decided to account for this spatial variation in the simultaneous impedance inversion as well as the rock-physics attributes derived therefrom.

Wavelets were extracted at the different wells marked in red in Figure 6 and interpolated in between them as provided in the commercial software packages. In Figures 23 and 24, we show a segment of an arbitrary line passing through two wells (W14 and W6) and drawn from V_P/V_S volumes, generated with a single angle-dependent wavelet (Figure 23) and with a spatial variation of angle-dependent wavelets (Figure 24). Similar sections drawn from S-impedance data volumes also showed differences at different levels.

Conclusion

Our endeavor in this whole exercise has been to bring in accuracy in the different zones constituting the rather large lithounits from Bone Spring to the Mississippian.

For this, we have paid attention to considerations such as addressing the noise content in the seismic data, accounting for the temporal and spatial variation of the wavelets embedded in the data, predicting shear wave curves using neural network analysis, generating an accurate multiregression attribute analysis-based low-frequency model, and using different facies trends in the individual inversion windows.These steps have addressed the issues that we raised at the beginning of the reservoir characterization exercise.

We firmly believe that all of these considerations have added interpretation value to the products that we have generated so far, and we make use of them for generating different characterization elements such as lithofacies classification, as discussed in part 2 of this paper.

Acknowledgements

The authors wish to thank TGS for encouraging this work and for the permission to present and publish it. The well data used in this work were obtained from the TGS Well Data Library and are gratefully acknowledged.

Data and materials availability

Data associated with this research are confidential and cannot be released.

References

Adams, J. E., M. G. Cheney, R. K. Deford, R. I. Dickey, C. O. Dunbar, J. M. Hills, R. E. King, E. R. Llyod, A. K. Miller, and C. E. Needam, 1939, Standard Permian section of North America: AAPG Bulletin, **23**, 1673–1681.

Castagna, J. P., M. L. Batzle, and R. L. Eastwood, 1985, Relationship between compressional-wave and shear-wave velocities in clastic silicate rocks: Geophysics, **50**, 571–581, doi: 10.1190/1.1441933.

Chapa, S., 2018, United States now the largest global crude oil producer, published on September 12, 2018, https://www.bizjournals.com/sanantonio/news/2018/09/12/united-states-now-the-largest-global-crude-oil.html, accessed 27th November 2018.

Dix, C. H., 1955, Seismic velocities from surface measurements: Geophysics, **20**, 68–86, doi: 10.1190/1.1438126.

Greenberg, M. L., and J. P. Castagna, 1992, Shear-wave velocity estimation in porous rocks: Theoretical formulation, preliminary verification and applications: Geophysical Prospecting, **40**, 195–209, doi: 10.1111/j.1365-2478.1992.tb00371.x.

Hampson, D., J. S. Schuelke, and J. A. Quirein, 2001, Use of multi-attribute transforms to predict log properties from seismic data: Geophysics, **66**, 220–236, doi: 10.1190/1.1444899.

Hampson, D. P., B. H. Russell, and B. Bankhead, 2005, Simultaneous inversion of prestack seismic data: 75th Annual International Meeting, SEG, Expanded Abstracts, 1633–1637, doi: 10.1190/1.2148008.

Hill, C. A., 1996, Geology of the Delaware basin—Guadalupe, Apache, and Glass Mountains, southeastern New Mexico and west Texas: SEPM Permian Basin Section, Publication 96-39.

Hills, J. M., 1984, Sedimentation, tectonism, and hydrocarbon generation in Delaware Basin, West Texas and southeastern New Mexico: AAPG Bulletin, **68**, 250–267.

Keller, G. R., J. M. Hills, and R. Djeddi, 1980, A regional geological and geophysical study of the Delaware basin. New Mexico and West Texas, in Trans-Pecos region: New Mexico Geological Society Guidebook, 31st Field Conference, 105–111.

Krief, M., J. Garat, J. Stellingwerff, and J. Ventre, 1990, A petrophysical interpretation using the velocities of P and S waves (full waveform sonic): The Log Analyst, **31**, 355–369.

Margrave, G. F., 2013, Why seismic-to-seismic ties are difficult, CREWES: Research Report, **25**, 1–26.

Mukhopadhaya, P. K., and S. Mallick, 2011, An accurate ray-based offset-to-angle transform from normal moveout uncorrected multicomponent data in a transversely isotropic medium with vertical symmetry axis: Geophysics, **76**, C41–C51, doi: 10.1190/1.3565182.

Ray, A. K., and S. Chopra, 2016, Building more robust low-frequency models for seismic impedance inversion: First Break, **34**, 29–34.

Walden, A. T., 1991, Making AVO sections more robust: Geophysical Prospecting, **39**, 915–942, doi: 10.1111/j.1365-2478.1991.tb00350.x.